

# JGR Atmospheres

## RESEARCH ARTICLE

10.1029/2024JD042393

### Key Points:

- Three distinct nocturnal convection episodes are observed ahead of a squall line, with one of them evolving into a supercell
- The supercell is elevated, locates at the terminus of the low-level jet (LLJ) and at the entrance of mid-tropospheric jet
- The LLJ significantly destabilizes the environment above an inversion layer, favoring the initiation of the supercell

### Correspondence to:




Y. Du,  
duyu7@mail.sysu.edu.cn

### Citation:

Yang, H., Du, Y., & Sun, J. (2025). The merger of a supercell and squall line in the Great Plains. 1: Initiation of the supercell. *Journal of Geophysical Research: Atmospheres*, 130, e2024JD042393. <https://doi.org/10.1029/2024JD042393>

Received 4 SEP 2024  
Accepted 30 MAY 2025

## The Merger of a Supercell and Squall Line in the Great Plains. 1: Initiation of the Supercell

Hongpei Yang<sup>1</sup> , Yu Du<sup>1,2,3</sup> , and Juanzhen Sun<sup>4</sup> 

<sup>1</sup>School of Atmospheric Sciences, Sun Yat-sen University, and Southern Marine Science and Engineering Guangdong Laboratory (Zhuhai), Zhuhai, China, <sup>2</sup>Guangdong Province Key Laboratory for Climate Change and Natural Disaster Studies, Sun Yat-sen University, Zhuhai, China, <sup>3</sup>Key Laboratory of Tropical Atmosphere-Ocean System, Sun Yat-sen University, Ministry of Education, Zhuhai, China, <sup>4</sup>National Center for Atmospheric Research, Boulder, CO, USA

**Abstract** Using a four-dimensional variational data assimilation system that incorporates radar and surface observations, we investigated the initiation mechanism of a nocturnal supercell in the central Great Plains on 23 May 2020. This pristine convection occurred ahead of an eastward-propagating squall line, despite the absence of discernible surface convergence, and later evolved into a supercell that eventually merged with the approaching squall line. The atmospheric environment, which featured a low-level inversion layer with considerable convective inhibition, was generally unfavorable for surface-based convective initiation (CI). However, our analysis indicated that the spatial heterogeneous nocturnal southerly low-level jet (LLJ) played a key role in the elevated CI. As the LLJ advected moisture and warm air, neighboring regions experienced substantial low-level destabilization. Multiple convergence bands associated with the heterogeneous LLJ were identified, and the timing and location of CI were governed by these bands. CI occurred when one of the convergence bands moved northward to a position beneath a divergence band at the entrance of the mid-tropospheric jet. This overlapping pattern of convergence-divergence persisted for over an hour, facilitating both the initiation and development of the supercell. Additionally, we observed two other episodes of CI ahead of the squall line, each with different characteristics. The first, occurring earlier than the supercell initiation, was triggered by topographic convergence in a valley but quickly dissipated. Later, as the LLJ rotated clockwise, the most prominent convergence band shifted eastward, favoring the continuous development of forward-building cells ahead of the squall line, resulting in a T-shaped system.

**Plain Language Summary** Understanding and forecasting nighttime thunderstorms over the United States Great Plains has always been a great challenge. A key factor contributing to storm initiation is the nocturnal low-level jet (LLJ). To better understand the varying impacts of the LLJ on storm initiation, this study explores the diverse structure of the LLJ and demonstrates how multiple convergence bands are generated and evolve due to LLJ heterogeneity. Using advanced radar and surface data assimilation, we observe that in addition to supplying unstable energy, the LLJ can couple with mid-tropospheric jet, creating persistent uplift that forms storms. Our findings highlight the importance of understanding the three-dimensional structure of the LLJ and may lead to improved forecast of nighttime rainfall.

## 1. Introduction

During the warm season, the precipitation over the U.S. Great Plains exhibits a pronounced nocturnal maximum (Wallace, 1975). This nocturnal precipitation is largely attributed to mesoscale convective systems (MCSs) (Fritsch et al., 1986; Maddox, 1980), including both pre-existing MCSs initiated before sunset that propagate through the Great Plains overnight, and nocturnal convective initiation (NCI) events in this region (Carbone et al., 2002; Carbone & Tuttle, 2008). During the Plains Elevated Convection at Night field campaign (PECAN) (Geerts et al., 2017), NCI contributed significantly to nocturnal rainfall, accounting for 30%–60% of the total. NCI events can have a high impact by producing severe weather such as hails and high winds (Reif & Bluestein, 2017, 2018).

Despite recent improvements in observations and numerical simulations, accurately forecasting NCI remains challenging (Davis et al., 2003; Surcel et al., 2010; Trier et al., 2006). Unlike daytime CI that often occurs near surface boundaries, NCI typically occurs at higher altitudes above the boundary layer due to the development of near-surface stable layer after sunset (e.g., Wilson & Roberts, 2006). Atmospheric conditions at these altitudes (i.e., 900–600 hPa) are inadequately represented in current real-time observation systems, leading to limited

predictive cues for NCI forecasting. Additionally, NCI is closely related to mesoscale features such as low-level jet (LLJ), bores, and gravity waves, which are not accurately resolved in operational models (Trier et al., 2014).

Previous studies have demonstrated the significant role of the nocturnal LLJ in supporting NCIs and their development into MCSs (Maddox, 1980, 1983). For example, a 20-year climatology of NCI by Reif and Bluestein (2017) indicated that over 70% of NCI events in the Great Plains are associated with the LLJ. Convergence often occurs at the northern terminus of the LLJ, strongly linking NCI to this region (Astling et al., 1985; Pitchford & London, 1962; Trier et al., 2006, 2014, 2020; Tuttle & Davis, 2006). As the night progresses, the clockwise veering of the LLJ driven by the inertial oscillation mechanism (Blackadar, 1957) shifts convergence toward the eastern flank of the LLJ, potentially assisting in the organization of convective storms (Bonner, 1966). In addition to dynamical support from LLJ convergence, the LLJ advects abundant warm and moist air northward, providing thermodynamic support (Higgins et al., 1997; Rasmusson, 1967). The nocturnal LLJ may also destabilize the environment (Du et al., 2022). Even in the presence of a near-surface layer with considerable convective inhibition (CIN), the LLJ can lift air to its level of free convection, promoting CI via transporting moist static energy over sloping isentropic surfaces of fronts (Trier & Parsons, 1993).

Typically, the Great Plains LLJ reaches its maximum strength at around 0100 LST (UTC-5, Daylight Saving Time) in the warm-season (Jiang et al., 2007; Pu & Dickinson, 2014). However, a portion of NCI events occurs earlier (e.g., Figure 3b in Reif & Bluestein, 2017), suggesting that the timing of NCI may not solely depend on the magnitude of LLJ convergence.

The LLJ can interact with winds at higher levels to support NCI. Several previous studies suggested that the LLJ is coupled with the upper tropospheric jet streak at 250 hPa, which intensifies the LLJ through its transverse circulation generated due to ageostrophic adjustment (Burrows et al., 2020; Uccellini & Johnson, 1979). With the LLJ advecting warm and moist air, warm-season elevated MCSs are often located within the right-entrance region of the upper-level jet, where divergence is maximized (Moore et al., 2003). Additionally, the LLJ in the boundary layer facilitates NCI by cooperating with a synoptic jet at higher altitudes (~1–4 km) in South China (Du & Chen, 2019). NCI is favored when divergence at the synoptic jet's entrance overlaps with convergence at the exit of the LLJ within the boundary layer (Liu et al., 2020; M. Zhang & Meng, 2019). This controlling mechanism has also been confirmed in other regions, such as Taiwan (G. T.-J. Chen et al., 2005), North and Southwest China (Luo & Du, 2023; F. Zhang et al., 2019), and Yangtze river basin (Cui et al., 2023). Recently, Trier et al. (2020) examined an NCI case during PECAN, demonstrating that while the LLJ influenced the timing of NCI through enhancing convergence, the NCI developed beneath the mid-tropospheric jet (MTJ) streak, suggesting a potential role for the MTJ. However, the coupling mechanism between the LLJ and the MTJ over the Great Plains remains an open question.

The Great Plains LLJ exhibits strong heterogeneity in terms of depth, wind speed, and direction. Using PECAN observations and model forecasts, Gebauer et al. (2018) showed that this heterogeneity not only led to differential moisture advection within the area but also increased convergence in regions other than the northern terminus, thus promoting NCIs. Additionally, the LLJ heterogeneity evolves as it moves across the Great Plains through the night, suggesting inherently correlated spatial and temporal characteristics (Smith et al., 2019). Given the significant warm advection associated with the LLJ, it is reasonable to hypothesize that LLJ heterogeneity may feedback on the MTJ, complicating their coupling processes. With the approach of convective systems, the evolution of both the LLJ and MTJ may vary. Hence, investigations into the spatiotemporal variability of the LLJ and its connection to the MTJ, as well as their implications for NCI, are warranted.

In this study, we aim to shed light on these questions by examining an NCI event that occurred in the central Great Plains on 23 May 2020. It subsequently developed into a supercell that produced multiple hail events before merging with an eastward-propagating squall line, forming a severe bow echo after merging. The initiation of the supercell serves as the prerequisite for this canonical storm merger, highlighting the need to investigate the key mechanisms governing its location and timing. We employ the Variational Doppler Radar Analysis System (VDRAS) (Sun & Crook, 1997) to analyze how the heterogeneous LLJ contributes to NCI episodes ahead of the squall line. In Part 1 of the study, we focus on the initiation of a supercell while the merging process will be discussed in Part 2.

The rest of the paper is organized as follows. Section 2 provides a brief overview of VDRAS and validates its performance in producing reliable dynamical and thermodynamic fields. Section 3 describes the three distinct

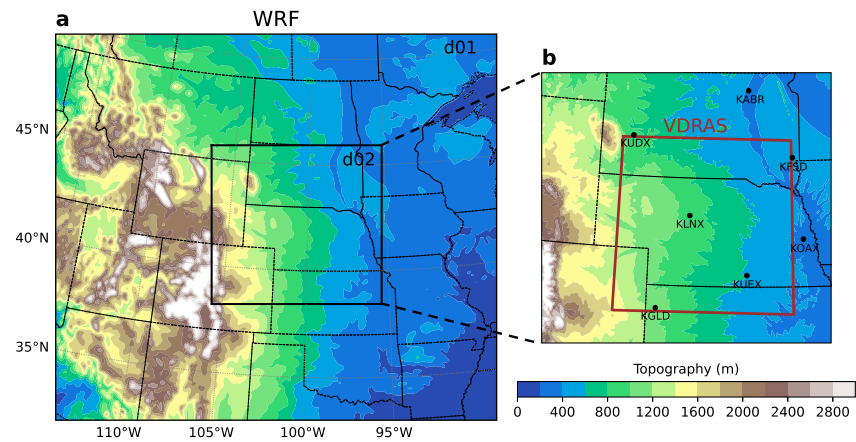


**Figure 1.** Domain configuration of (a) weather research and forecasting (WRF) and (b) variational doppler radar analysis system (VDRAS). The locations of the seven next generation weather radar radars used in VDRAS are marked in (b) with text labels.

NCI episodes and their synoptic background. Section 4 examines the temporal and spatial evolution of the nocturnal LLJ and investigates how the LLJ produced different NCI episodes. Additionally, this section discusses how MTJ responds to intensifying LLJ and contributes to supercell initiation through LLJ-MTJ coupling. Finally, Section 5 presents the main conclusions.

## 2. VDRAS Description and Validation

Based on the four-dimensional variational data assimilation (4DVar) technique, VDRAS (Sun & Crook, 1997) is a system proficient in severe weather analyses. Over the past two decades, it has been applied in regions throughout the world to reveal meso- and convective-scale processes vital for the initiation and development of convective systems (e.g., Chang et al., 2016; Sun et al., 2023; Tai et al., 2017). By assimilating reflectivity and radial velocity from Doppler radars along with surface observations, VDRAS can retrieve four-dimensional mesoscale dynamical and thermodynamic fields with frequent updates (typically every 5–15 min). In addition to the data assimilated, VDRAS incorporates large-scale background information from Weather Research and Forecasting (WRF) model simulations as initial guess background and boundary conditions. VDRAS outputs three-dimensional gridded high-resolution meteorological variables (such as wind, pressure, humidity, temperature, etc.) and a number of diagnosed fields, including horizontal divergence, vorticity, convective available potential energy (CAPE), and CIN, enabling comprehensive investigation into the key processes driving supercell initiation in this study.

The latest version of VDRAS (X. Chen et al., 2016; Tai et al., 2017) was used, with its domain centered at 41.65°N, 100.0°W, covering an area of 540 × 540 km<sup>2</sup> with a horizontal grid spacing of 3 × 3 km (Figure 1b). The VDRAS domain comprised 40 vertical layers with a vertical grid spacing of 250 m, and the lowest model level was set at 125 m. The 4DVar analysis was conducted from 1900 to 0300 LST on 23–24 May 2020 for the entire event, with assimilation performed every 10 min using a 10-min assimilation window length. Radial velocity and reflectivity from seven S-band Doppler radars of the Next Generation Weather Radar (NEXRAD) with approximately 6-min scan intervals, and surface observations from Automated Surface Observing System (ASOS) at 5-min interval, were assimilated (Figure 1b). Due to a significant amount of missing data before 2200 LST, surface data were only assimilated during the subsequent five hours. Since VDRAS uses a constant height vertical coordinate, the surface data were matched to the nearest vertical level prior to their assimilation.

The Advanced Research version of WRF was employed with a one-way nested configuration of two domains (Figure 1a). The horizontal grid spacings for the outer and inner domains are 9 and 3 km, respectively. The physics schemes applied are detailed in Table 1. Similar to the method performed in Sun et al. (2023), we initialized WRF forecasts using NCEP Global Forecasting System (GFS) analysis every 3 hr, and the output was written out at 30 min intervals. The WRF 3 km forecast between 3 and 6 hr, with the valid time closest to the analysis time (either 3, 3.5, 4, 4.5, 5, or 5.5 hr), was used to drive VDRAS assimilation by providing boundary

**Table 1**  
WRF Physics Schemes Configuration

Physics schemes	Option
Microphysics	Thompson
Longwave radiation	RRTMG
Shortwave radiation	Dudhia
Planetary boundary layer	Mellor-Yamada-Janjic
Surface layer	Revised MM5
Land surface model	Noah
Cumulus parameterization	Kain-Fritsch (only d01)

condition and first guess fields. Note that the 3–6 hr forecast, rather than the 0–3 hr WRF forecast, was used to avoid the spin-up issue of the WRF forecast.

The accuracy of VDRAS analysis has been extensively evaluated in previous studies by comparing analysis fields and diagnosed parameters with various observations, including surface observation, dual-Doppler radar synthesis, radiosonde, and aircraft data (Crook & Sun, 2004; Sun & Crook, 1998; Xiao et al., 2017; L. Zhang et al., 2021). A practical validation approach involves comparing the root mean square error (RMSE) of radial velocity between assimilated observations and VDRAS with that between assimilated observations and WRF background (L. Zhang et al., 2021). Figures 2a–2d display the mean RMSE for both VDRAS analyses and WRF counterparts during the CI and merger periods. Both the RMSE spread and the mean RMSE are

significantly reduced by 1–1.3 m s<sup>−1</sup> following assimilation in both stages, consistent with previous studies. Due to more widespread convective development within the VDRAS domain during the merger stage, the WRF RMSE spread is correspondingly larger than that in the CI stage, with the mean RMSE approximately 1 m s<sup>−1</sup> higher (Figures 1a and 1c). Specifically, for the radar closest to the bow echo (KLNK), RMSE is reduced from

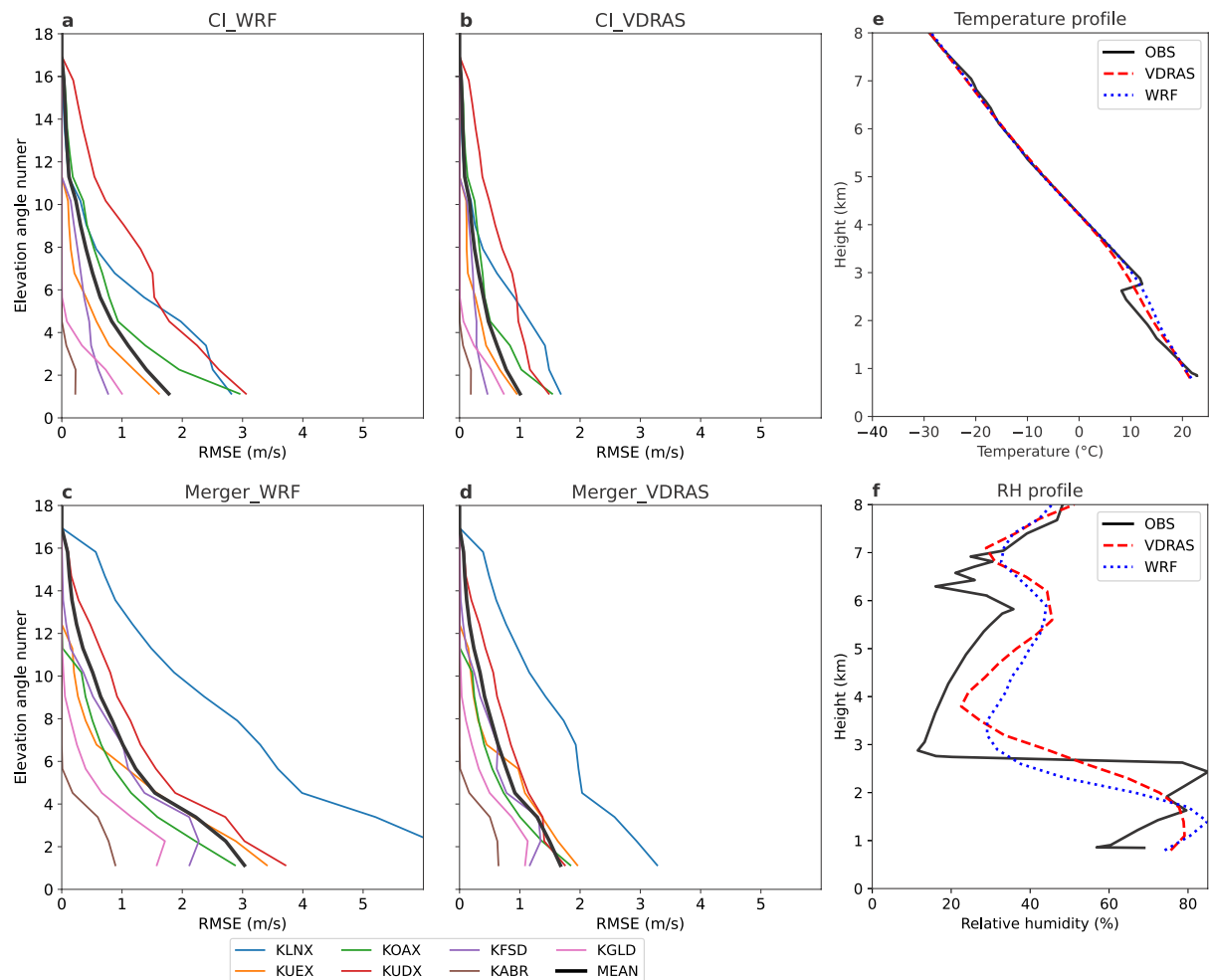


**Figure 2.** Root mean square errors (RMSE) of radial velocity (m s<sup>−1</sup>) calculated from (a) variational doppler radar analysis system (VDRAS) and (b) weather research and forecasting (WRF) background against observations during (a), (b) the convective initiation stage (1900–2220 LST) and (c), (d) merger stage (2220–0300 LST) for seven radars. The black lines delineate the mean RMSEs across all radars. Vertical profiles of (e) temperature (°C), and (f) relative humidity (%) from sounding observations (LBF), VDRAS, and WRF at 1900 LST.



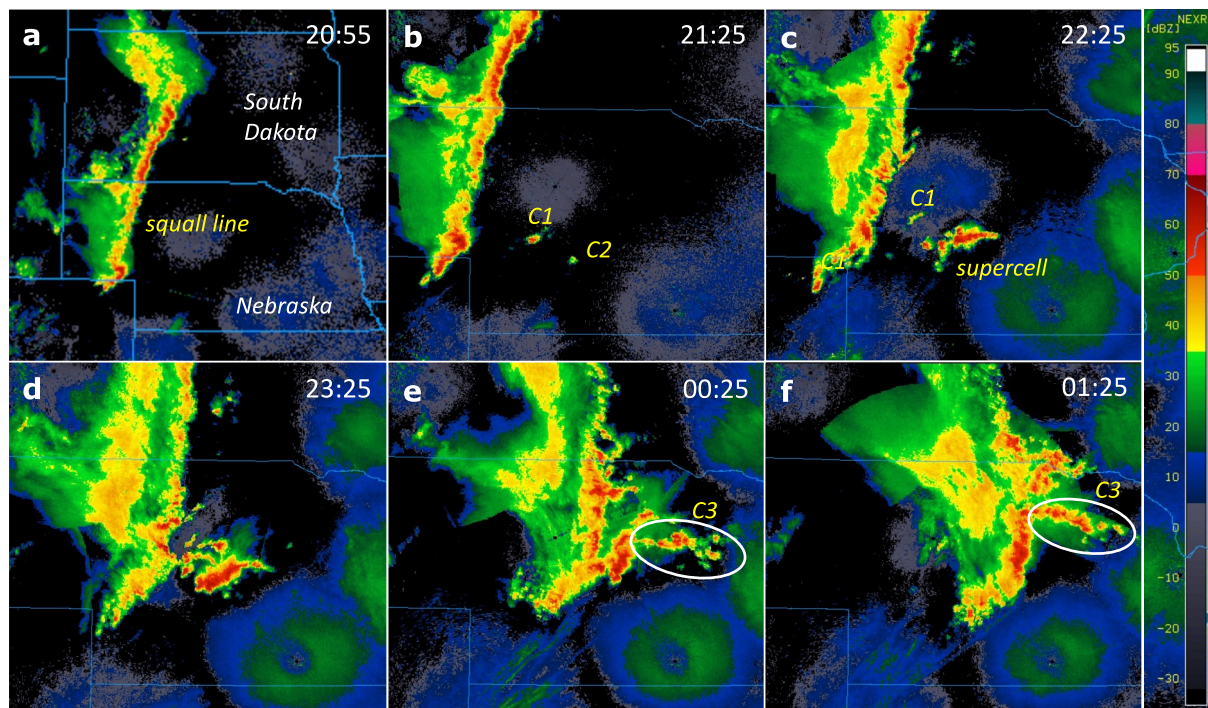


**Figure 3.** Radar composite (dBZ) at (a) 2055, (b) 2125, (c) 2225, (d) 2325, (e) 0025, and (f) 0125 LST on 23–24 May 2020 in the central Great Plains. The squall line, convective cells C1 and C2 (which developed into a supercell), and convective clusters of convective cells (C3) are labeled with text annotations.

$\sim 6.2 \text{ m s}^{-1}$  to  $\sim 3.5 \text{ m s}^{-1}$  during the merger stage. In addition, an independent sounding observation within the VDRAS domain, which was not assimilated, was used for further evaluation. Figures 2e and 2f show that while the WRF background underestimates moisture content and overestimates temperature below 3 km, VDRAS displays noticeable improvement after assimilation. The temperature bias is reduced from over  $4^\circ\text{C}$  to approximately  $2.5^\circ\text{C}$ , and the mean relative humidity between 1.5 and 3 km increases from  $\sim 50\%$  to  $\sim 60\%$ . Consequently, the optimal fit to radar and observations, coupled with background information provided by WRF, ensures that VDRAS analysis aligns closely with observations and could be confidently used for the following investigation in this event.

### 3. Overview of Convection Initiation on 23–24 May 2020

#### 3.1. Convection Initiation Episodes

On 23 May 2020, a 300 km-long squall line swept across the central Great Plains overnight (Figure 3). Ahead of it, three types of convection emerged, each initiated in distinctly different ways (C1–C3). A single cell, C1, located approximately 100 km east of the squall line, was initiated at 2104 LST (not shown), and then quickly grew to exceed 50 dBZ before dissipating within an hour (Figures 3b, 3c, and 4). The VDRAS analysis indicates that C1 resulted from the interaction of wind and topography, as near-surface southeasterlies decelerated along the terrain, generating a mesoscale convergence belt (Figure 5a).

In contrast to C1, another convective cell, C2, positioned further east ( $\sim 150$  km away from the squall line), initiated without clear surface convergence 10 min later. Additionally, C2 was first observed by a relatively higher elevation angle scan of the radar (Figures 4a and 4b), suggesting it might be elevated (which will be further examined via parcel trajectories later). C2 was also identified as a pristine CI event that is unaffected by neighboring storms (Reif & Bluestein, 2017), as the distance between C2 and the gust front of the squall line exceeded the Rossby radius of deformation ( $\sim 100$  km). In the following hours, C2 rapidly evolved into a supercell with a typical hook echo and mesocyclone (Figures 4c and 4d). The supercell subsequently merged with the squall line to produce a bow echo and more severe weather, which will be discussed in Part 2. Hence, understanding the CI processes of C2 is the focus of this study, as it represents a prerequisite for the formation of the bow echo.

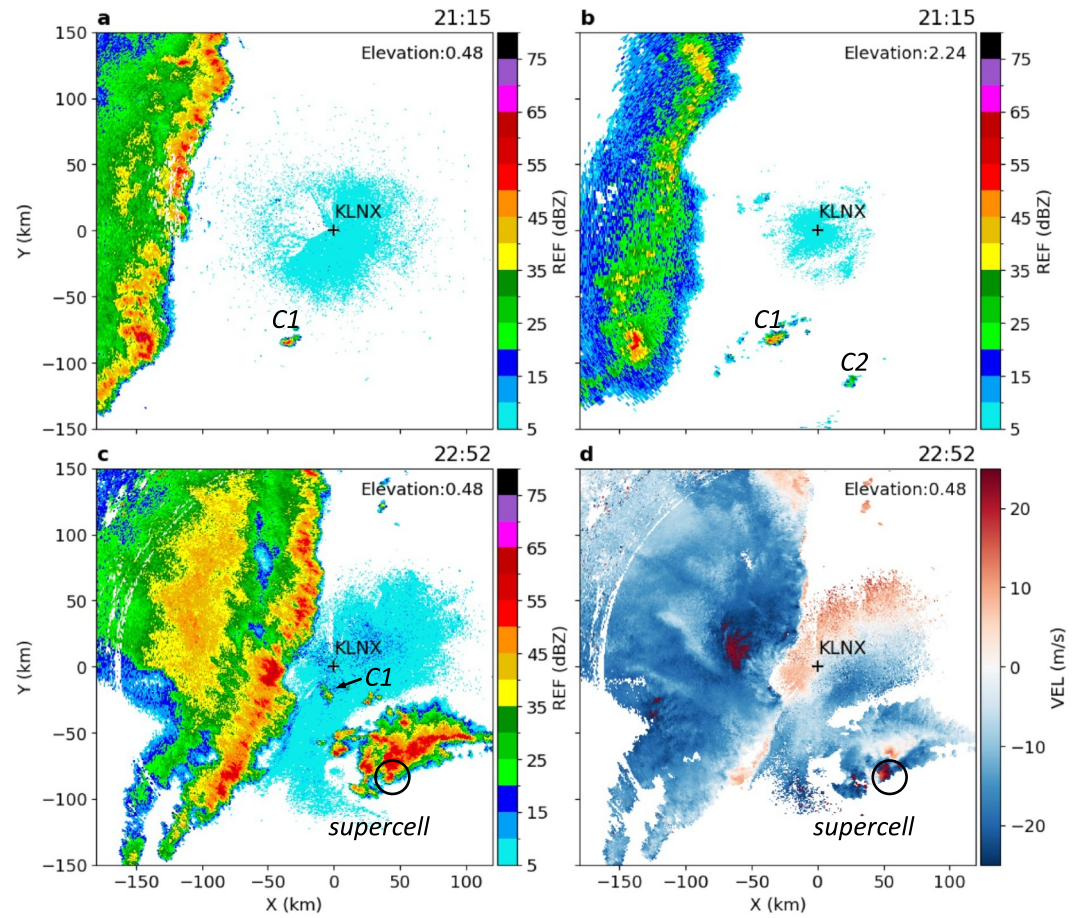


**Figure 4.** Observed (a–c) radar reflectivity (dBZ) and (d) radial velocity ( $\text{m s}^{-1}$ ) at (a), (b) 2115 and (c), (d) 2252 LST by KLN radar. The elevation angle of each subplot is indicated in the upper right corner, respectively.

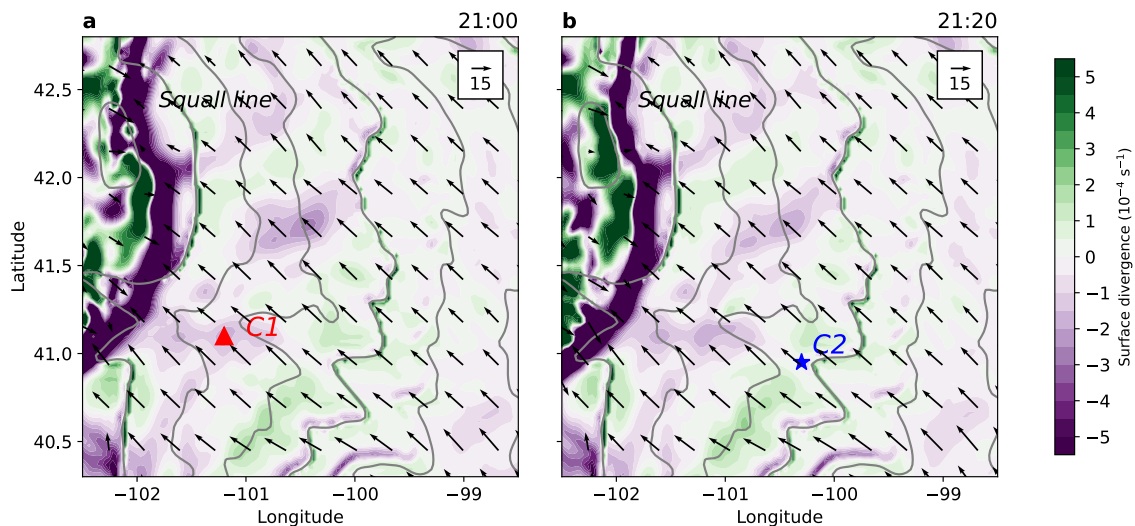


**Figure 5.** Distribution of variational doppler radar analysis system surface divergence (shading,  $\text{s}^{-1}$ ) at (a) 2100 and (b) 2120 LST, with topography (gray contours) overlaid at 100 m interval. The location of squall line, C1 and C2 are marked by black text, red triangle, and blue star, respectively.



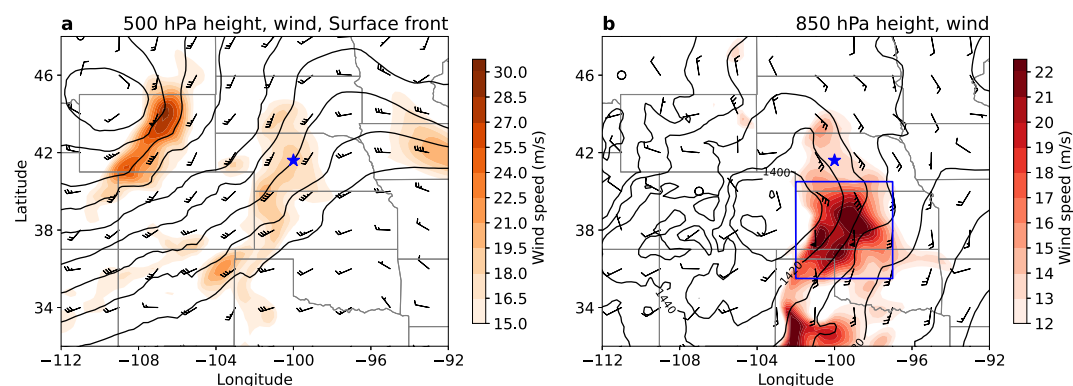


**Figure 6.** Synoptic pattern at 2100 LST on 23 May 2020, using ERA5 reanalysis. Geopotential height (black contours, gpm), full wind speed (shading, m s<sup>-1</sup>), and wind barbs at (a) 500 hPa and (b) 850 hPa. A full line on wind barbs represents 5 m s<sup>-1</sup>, and a flag represents 25 m s<sup>-1</sup>. The blue stars indicate the convective initiation location of supercell (C2), and the blue box in (b) indicates low-level jet and is used in Figure 8.

In addition to C1 and C2, a cluster of convective cells (C3) with T-shaped characteristic, known as T-initiation type (Coniglio et al., 2011; Weckwerth et al., 2019), occurred ahead of the main system later during 0000–0300 LST (Figures 3e and 3f). They formed in a line nearly perpendicular to the gust front of the cold pool. Previous studies suggested that their occurrence is often supported in an environment with large-scale horizontal deformation and is associated with warm advection near the LLJ terminus (Augustine & Caracena, 1994; Trier et al., 2017; Weckwerth et al., 2019). After 0130 LST, due to the eastward propagation of the main system, C3 was absorbed and revitalized the northern convective updraft of the main system (as indicated by a significant enhancement in radar reflectivity, not shown).

### 3.2. Synoptic Background

Based on the hourly fifth generation ECMWF reanalysis (ERA5) data with a spatial resolution of 0.25° × 0.25°, the synoptic conditions are depicted in Figure 6. At 2100 LST, a deep trough and a ridge were located on either side of the Great Plains at 500 hPa, with southwesterly winds dominating over Nebraska, where the NCI occurred (Figure 6a). Although with a relatively weak strength (16–18 m s<sup>-1</sup>), a MTJ was also observed near the location of C2. Accordingly, the presence of a surface cyclone was noted, and C2 was found to evolve above the surface warm front (not shown). Accompanying the strong 850 hPa low vortex, a significant LLJ with maximum wind speed exceeding 24 m s<sup>-1</sup> was observed. The LLJ can advect warm air and transport abundant moisture northward to the region of interest. Notably, C2 occurred at the northern terminus of the LLJ after sunset (Figure 6b), indicating its close relationship with the nocturnal LLJ enhancement, a common feature over the Great Plains.

The soundings closest (and prior) to the CI time indicate that the pre-CI environment was characterized by a dry layer between 500 and 750 hPa and relatively moist lower layers, contributing to strong instability (Figure 7). The nearest site, LBF, displayed a CAPE of 1,372.7 J kg<sup>-1</sup> (Figure 7a) while the most unstable CAPE exceeded 2,562 J kg<sup>-1</sup>. However, both the LBF and OAX soundings demonstrate the presence of a low-level nocturnal inversion layer, which produced moderate to large CIN. Due to weaker wind speed and associated warm advection at lower levels (Figure 6b), a smaller CAPE (745.5 J kg<sup>-1</sup>) and a larger CIN were observed (−136.5 J kg<sup>-1</sup>) in eastern Nebraska. This inversion layer was a remnant of the deep inversion layer from the previous night, which extended from the surface to 750 hPa (not shown). Although daytime solar heating gradually eroded it, the inversion layer did not fully dissipate by sunset and deepened again in the evening. Its persistent presence likely contributed to the suppression of daytime convection. Further discussion on changes in environment stability before CI is provided in Section 4.2. The wind profiles are generally representative of organized convective systems (e.g., squall lines and supercells). The hodograph measured from the LBF profile exhibited strong (>20 m s<sup>-1</sup>) and deep-layer (0–6 km AGL) shear while the 0–6 km shear from the OAX profile

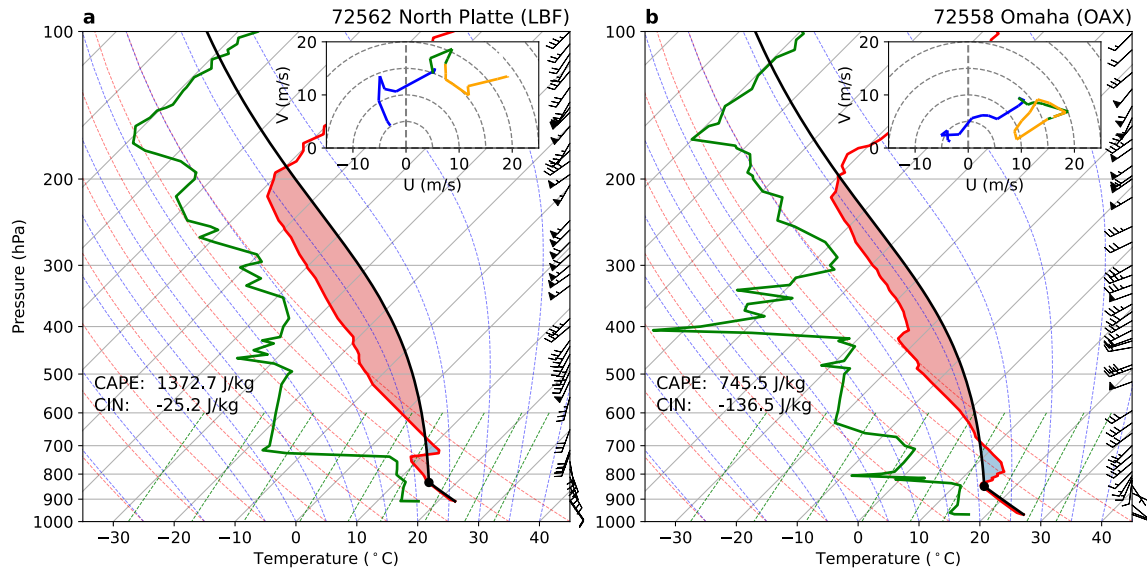


**Figure 7.** Skew T–logp diagrams at (a) North Platte and (b) Omaha site (as indicated by KLNK and KOAX in Figure 1) valid at 1900 LST on 23 May 2020, with wind hodographs for the lowest 12 km AGL shown in the upper right subplots. The color scheme on the hodographs represents the 0–3 (blue), 3–6 (green), and 6–12 km (yellow) layers.

reached  $\sim 25 \text{ m s}^{-1}$ . Additionally, VDRAS analysis shows that the 0–3 km shear near the C2 location exceeded  $25 \text{ m s}^{-1}$  (not shown), suggesting an environment supportive of mesocyclone development within the supercell.

In summary, this late spring event combined frontal dynamics, featuring an upper-level trough, ridge, and low-level vortices, along with LLJ activity, high temperatures, and abundant moisture, reflecting a blend of cold-season and warm-season convective characteristics.

#### 4. Nocturnal Convection Initiation Associated With Low-level Jet

Despite the favorable synoptic background for convective development, the isolated initiation of the supercell remains perplexing, as does the determination of its location. Hence, in this section, we will conduct a detailed examination of the controlling LLJ and the associated mesoscale processes triggering the NCI.

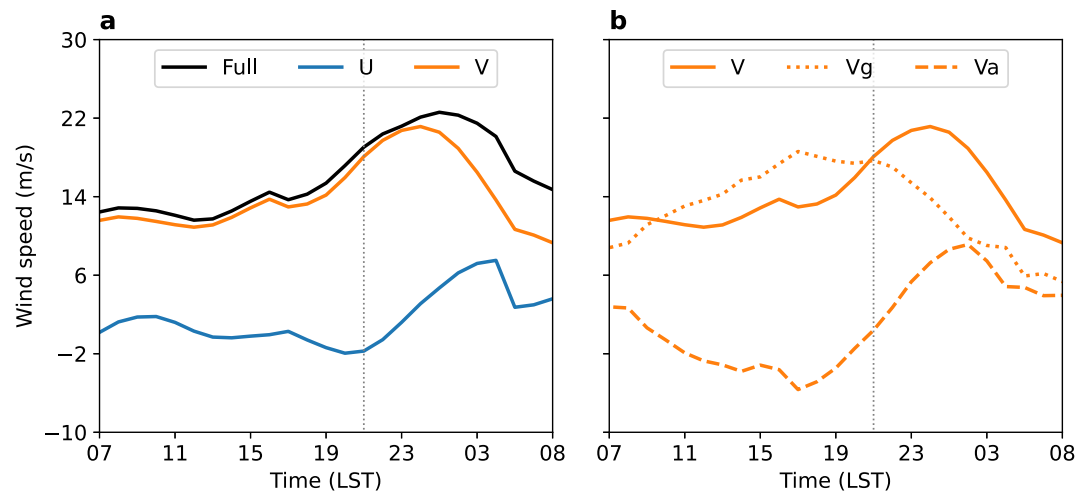


**Figure 8.** Evolution of (a) the full wind magnitude, u, v wind components and (b) geostrophic and ageostrophic wind components of the low-level jet at 850 hPa using ERA5 reanalysis. The timing of supercell initiation (2120 LST) is denoted by vertical gray dotted lines.



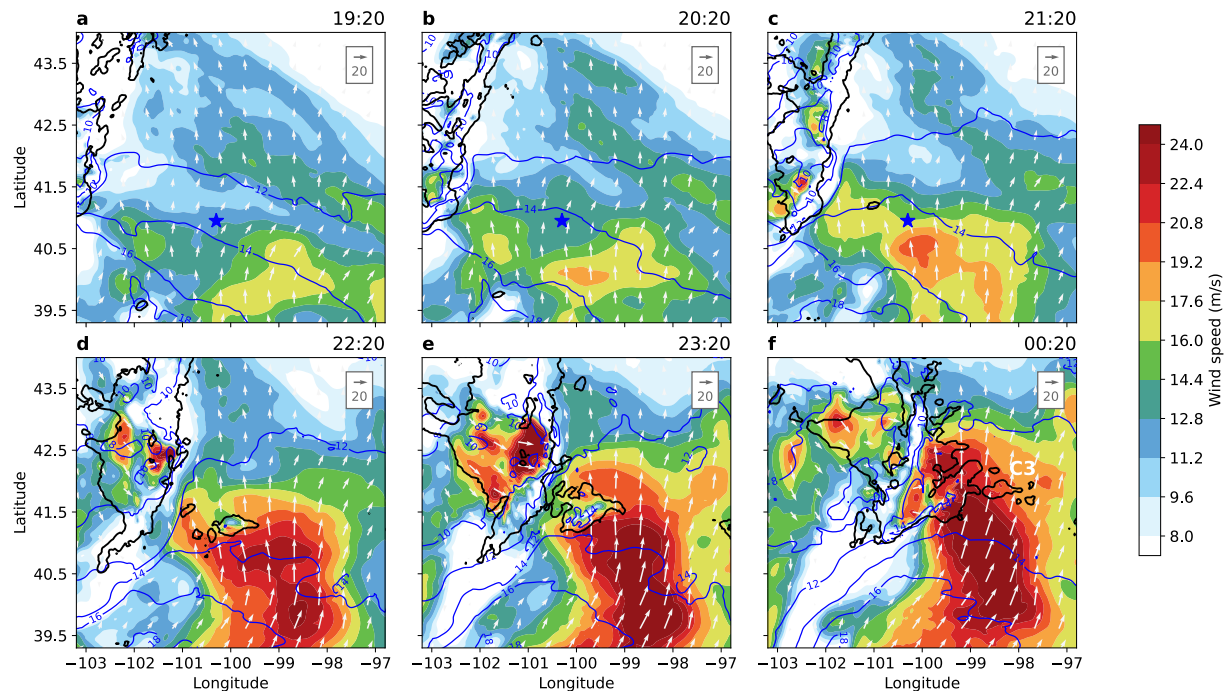


**Figure 9.** Distribution of variational doppler radar analysis system wind speed (shading,  $\text{m s}^{-1}$ ), wind vectors, and temperature (blue contours,  $^{\circ}\text{C}$ ) at 1.3 km MSL at (a) 1920, (b) 2020, (c) 2102, (d) 2220, (e) 2320, and (f) 0020 LST on 23–24 May 2020. The composite radar reflectivity of 25 dBZ is delineated by black contours. The blue stars in (a–c) indicate the location of C2 and cluster of convective cells (C3) is marked by text.

#### 4.1. Evolution of the LLJ

Figure 8 shows the temporal evolution of the LLJ core area at 850 hPa (blue box in Figure 6b). The LLJ was primarily composed of the V component of the wind, with an average strength of  $12\text{--}13 \text{ m s}^{-1}$  during the daytime. However, the LLJ experienced a significant intensification ( $\sim 10 \text{ m s}^{-1}$ ) during the night, reaching its peak strength of  $\sim 23 \text{ m s}^{-1}$  at 0000 LST. We further decompose the V-wind into geostrophic ( $v_g$ ) and ageostrophic parts ( $v_a$ ) according to  $v_g = \frac{g}{f} \frac{\partial Z}{\partial x}$ ,  $v_a = v - v_g$ , where  $g$  is the gravitational acceleration,  $f$  is the Coriolis parameter and  $Z$  is the geopotential height. As shown in Figure 8b, the geostrophic wind component first exhibited a steady increase before sunset (about 2000 LST) and then decreased overnight. According to the expression of  $v_g$ , this change was closely related to the variations in horizontal gradient of geopotential height associated with the low vortex (Figure 6b). While slowly moving eastward, the vortex deepened during the day and weakened when night arrived (figure not shown). Consistent with previous findings, this nocturnal enhancement was mainly attributed to the ageostrophic wind component. The transition of the ageostrophic V-wind from weak northerly to strong southerly followed the Blackadar mechanism, emphasizing the role of the reduction in eddy viscosity in the boundary layer after sunset (Blackadar, 1957). The ageostrophic wind reached a maximum between 0200 and 0300 LST, aligning well with the theoretical value at  $40^{\circ}\text{N}$  (Du & Rotunno, 2014). However, the peak LLJ strength occurred 2 hours earlier due to the decaying of the low vortex. Interestingly, C2 did not occur when the LLJ was stronger as mostly documented in the climatology of warm-season NCI (Reif & Bluestein, 2017), but rather occurred earlier, at 2115 LST. As we will discuss later, it turns out that the horizontal structure of the LLJ, as well as the coupling between the LLJ and winds at higher levels, exerted a significant influence on the NCI.

The VDRAS analysis was employed to examine the horizontal distribution of the nocturnal LLJ as well as its temporal variation. As shown in Figure 9, in addition to the nocturnal development and northward movement, the LLJ exhibited spatially heterogeneity with respect to both wind speed and wind direction, especially prior to 2100 LST. Despite their relatively weaker intensities, multiple wind speed cores were observed within the VDRAS domain. While the prevailing winds were primarily southwesterlies, the LLJ core exhibited stronger southerlies (Figures 9a–9c). Such heterogeneity of the LLJ may arise from the uneven heating influenced by local topography

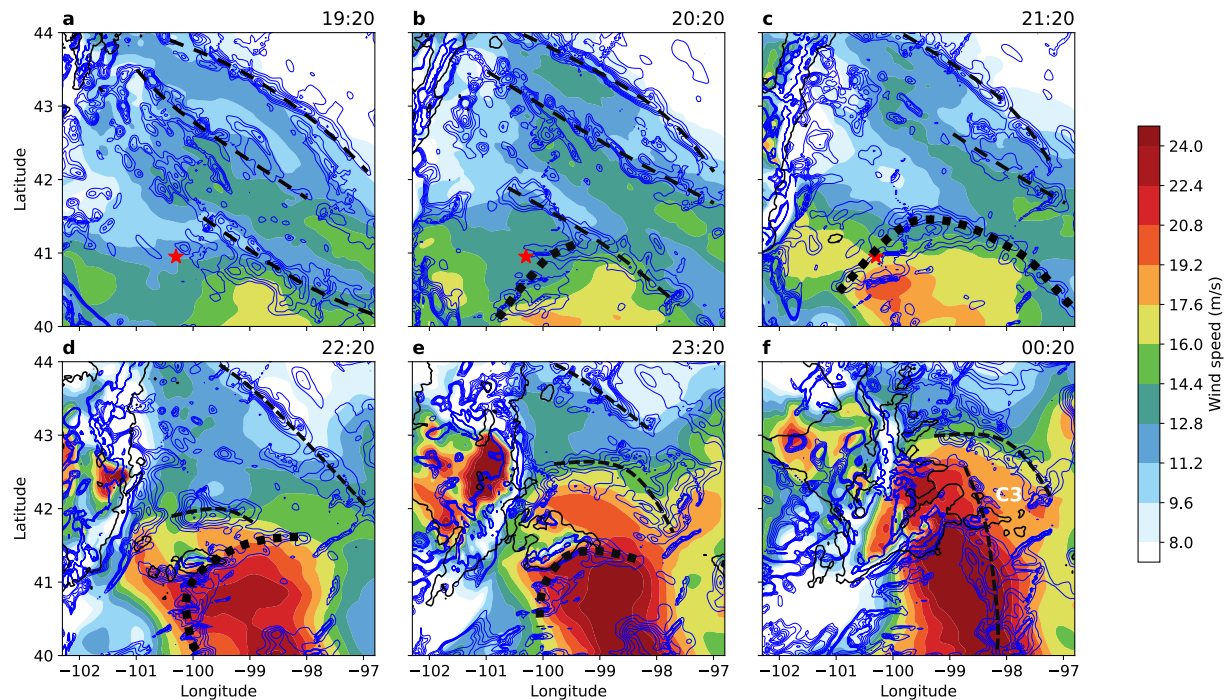


**Figure 10.** Distribution of variational doppler radar analysis system wind speed (shading,  $\text{m s}^{-1}$ ) and convergence (blue contours starting from  $-0.3 \times 10^{-5} \text{ s}^{-1}$  at an interval of  $-0.3 \times 10^{-5} \text{ s}^{-1}$ ) at 1.35 km AGL at (a) 1920, (b) 2020, (c) 2102, (d) 2220, (e) 2320, and (f) 0020 LST on 23–24 May 2020. The composite radar reflectivity of 25 dBZ is delineated by black contours. The red stars in (a–c) indicate the C2 location. Convergence bands are marked with black dashed lines, with the key convergence band shown by thick black dotted lines.

(Gebauer et al., 2018). However, this phenomenon became less evident as the LLJ strengthened (Figure 9), possibly due to the more pronounced effect of reduced turbulent mixing. A much stronger and more compact LLJ core was shown after 2320 LST, where the supercell developed in the left-exit region of the LLJ and C3 was found in the right-exit area (Figures 9e and 9f).

#### 4.2. Dynamic and Thermodynamic Effects of LLJ

The dynamic effect of LLJ on NCI has long been associated with LLJ-related horizontal convergence zone. Figure 10 suggests that downstream of the heterogenous LLJ, there were multiple localized convergence bands, which could be conducive to NCI. These convergence bands were parallel to the distribution of wind speed, indicating that they mainly originated from wind speed convergence. The convergence band of interest was associated with the strongest LLJ core. At 1920 LST, only a northwest-southeast oriented band existed to the east of the C2 location (Figure 10a). However, as the LLJ core shifted westward and greatly enhanced, a new convergence band to the south of C2 established (black dotted line in Figure 10b). It migrated northwestward with the LLJ and arrived at the C2 location at 2120 LST, indicating its role in triggering C2.

Due to the larger gradient of wind speed on the left side of the LLJ terminus, the convergence on this side was also stronger (Figure 10c). It persisted during 2120–2320 LST and facilitated the development of the supercell after CI, as indicated by the enlarging area of high radar reflectivity (Figures 10d and 10e). Later around midnight, another convergence band emerged on the right side of the LLJ terminus (Figure 10e). Figures 9e and 9b suggest that the formation of this band stemmed from the clockwise rotation of LLJ. The transition of southerlies to southwesterlies also resulted in the northeastward movement of the convergence band. Correspondingly, continuous initiation of forward cells (C3) and the resulting T-shaped system were observed (Figures 3e and 3f).

In addition to supplying convergence, LLJ advects moisture and warm air to improve the low-level environment, preconditioning it for NCI. Using VDRAS, we evaluated how the environment stability responded to the LLJ (Figure 11). VDRAS analysis suggests small to moderate CAPE and large CIN for air originating at 1.3 km AGL within the area of the LLJ and squall line prior to NCI (Figures 11a and 11d). As shown in Figure 11, the temporal

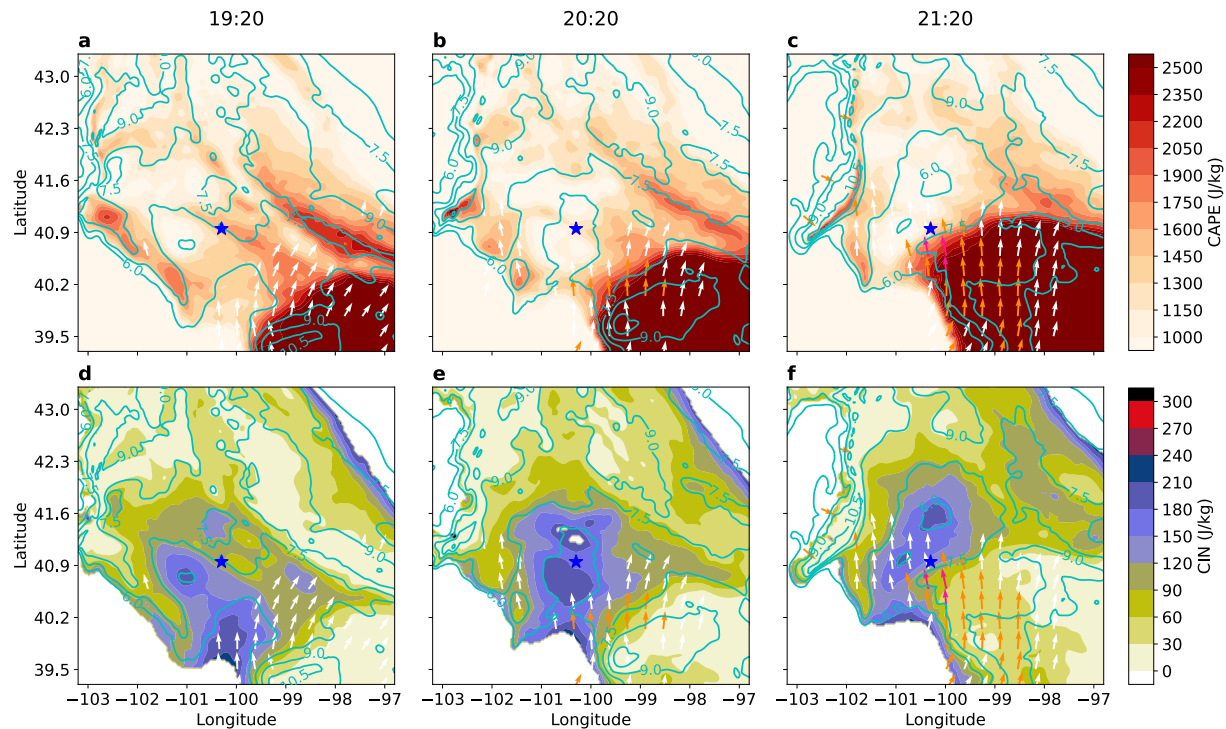


**Figure 11.** Distribution of convective available potential energy (CAPE) (shading,  $\text{J kg}^{-1}$ ), water vapor mixing ratio (contours,  $\text{g kg}^{-1}$ ), and wind vectors (white, orange, and pink vectors correspond to wind speeds exceed 15, 17, 19  $\text{m s}^{-1}$ , respectively) at 1.35 km AGL at (a) 1920, (b) 2020, and (c) 2120 LST on 23 May 2020 (d–f) are as in (a–c), but with convective inhibition (CIN) ( $\text{J kg}^{-1}$ ) shaded. The blue stars represent the location of C2. CIN is masked if CAPE is smaller than  $100 \text{ J kg}^{-1}$  in variational doppler radar analysis system.

variations in CAPE and CIN were primarily from the changes in water vapor content, instead of the change of temperature. Possibly due to the localized drying effect, the environment near C2 location even first exhibited a drop in CAPE and an increase in CIN before 2020 LST (Figures 11a, 11b, 11d and 11e). At 2020 LST, CIN was shown to exceed  $150 \text{ J kg}^{-1}$  while CAPE was below  $1150 \text{ J kg}^{-1}$ . Nevertheless, as the LLJ strengthened, more water vapor from the southeastern area was advected toward the area, destabilizing the cloud environment (Figures 11c and f). A decrease ( $\sim 30 \text{ J kg}^{-1}$ ) in CIN and a significant increase in CAPE ( $\sim 450 \text{ J kg}^{-1}$ ) were found near the C2 location as the LLJ expanded northwestward, illustrating the important role of LLJ in modifying the environmental instability and developing NCI.

### 4.3. Evolution of Mid-level Strong Winds and the LLJ-MTJ Coupling

While supercell initiation was favored by both the dynamical and thermodynamical effects of the LLJ, its timing and location were additionally influenced by the development of an MTJ. In contrast to the 500 hPa wind distribution in ERA5, VDRAS analysis provided more detailed insights into the horizontal structure and evolution of winds at the 4.05 km AGL, approximately corresponding to 600 hPa (Figure 12). Similar to the configuration of convergence bands associated with the heterogeneous LLJ, multiple divergence bands were present at the entrance of the unevenly distributed mid-level winds.

Figure 12a shows two major divergence bands at 1920 LST ahead of the squall line, with the western one featuring greater intensity in response to the greater change in wind speeds. Due to the eastward propagation of the squall line (as indicated by the propagation of the strongest divergence zone in Figure 12), a “convective jet” formed due to the approaching of the squall line that blocked mid-level airflows. This jet was most prominent at 2120 LST when the squall line remained compact (Figure 12c). However, the supercell was triggered much ahead of this jet, and hence seems more influenced by the MTJ that developed after 2020 LST (Figure 12b). This strong wind zone split from the original northwest-southeast oriented strong wind band (Figure 12a) and strengthened (Figure 12b), transitioning to a north-south orientation (Figures 12c and 12d) along with the divergence band at its entrance. By comparing the position of the MTJ area with that of the LLJ core, we observe a close match (both are



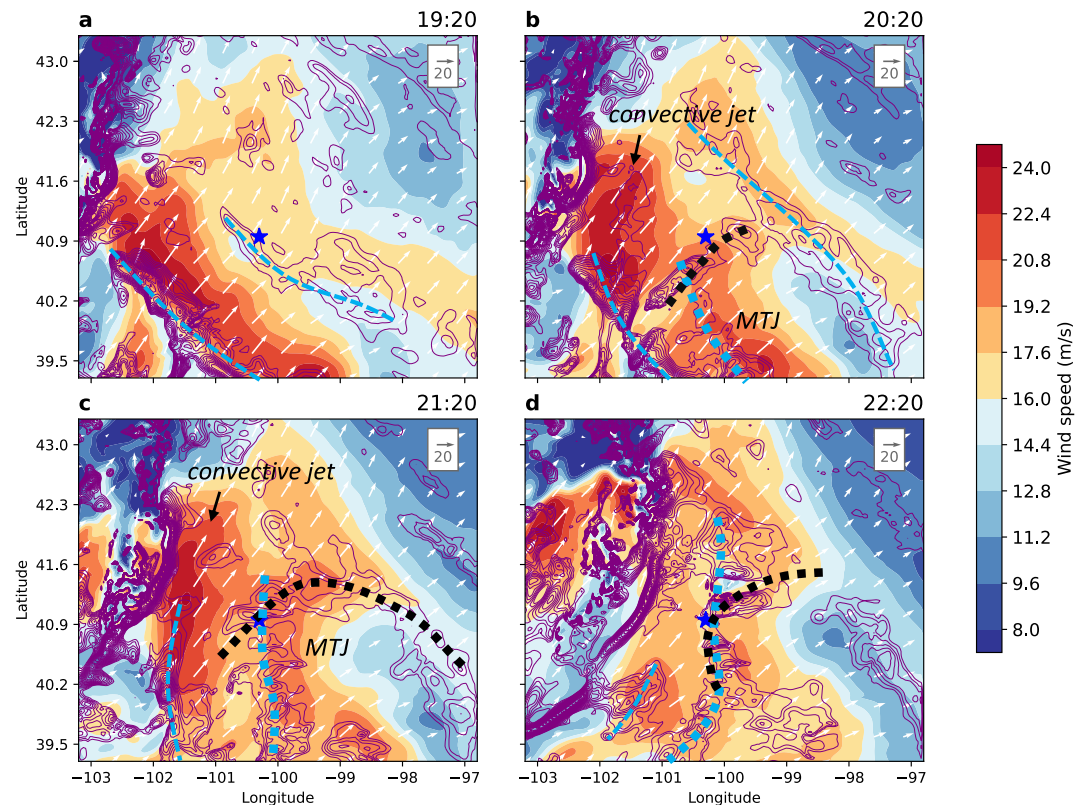


**Figure 12.** Distribution of variational doppler radar analysis system wind speed (shading,  $\text{m s}^{-1}$ ), wind vectors, and divergence (purple contours starting from  $0.3 \times 10^{-5} \text{ s}^{-1}$  at an interval of  $0.3 \times 10^{-5} \text{ s}^{-1}$ ) at 4.05 km AGL at (a) 1920, (b) 2020, (c) 2120, and (d) 2220 LST. The blue stars in (a–c) show the C2 location. Divergence bands are marked with blue dashed lines, with the primary divergence band highlighted by thick blue dotted lines. The black dotted line (key convergence) is reproduced from Figure 10.

at  $\sim 100^\circ\text{W}$ ), indicating that its formation is likely coupled with the evolution of LLJ. According to the thermal wind balance, the significant warm advection associated with the LLJ (Figure 9) may veer the low-level strong winds clockwise with height, contributing to the generation of the MTJ.

The 3D visualization presented in Figure 13 offers a comprehensive depiction of the configuration of LLJ and MTJ. It clearly shows that the nocturnal LLJ and the MTJ located in a basically consistent region, albeit with notable differences in wind directions. Additionally, while the LLJ induced mesoscale ascent in its terminus (Figure 14a), C2 was situated at the intersection of the LLJ terminus and the entrance of MTJ (Figure 13), underscoring the importance of their coupling.

Analyzing the movement of the low-level convergence band and mid-level divergence band, it becomes evident that these two lines started intersecting at around 2020 LST (Figure 12b). However, the occurrence of C2 was not observed at this time due to relatively weak divergence and convergence. It is only at 2120 LST when both divergence and convergence enhanced, that C2 emerged. Subsequently, the divergence band overlapped the western part of convergence band, suggesting sustained lifting during the period from 2120 to 2220 LST (Figure 12d). Therefore, we conclude that this unique arrangement of the nocturnal LLJ with the MTJ contributed to the initiation of the pristine supercell.

#### 4.4. Elevated Convection Initiation

As discussed, the initiation of the supercell did not originate from the surface due to significant CIN and divergence in the near-surface layer (Figures 5, 7, 14b). Instead, it likely began as elevated convection from a higher altitude, potentially facilitated by the LLJ. Vertical cross-sections along a line parallel to the LLJ further reveal a deep convergence layer associated with the LLJ and a divergence layer higher aloft in conjunction with



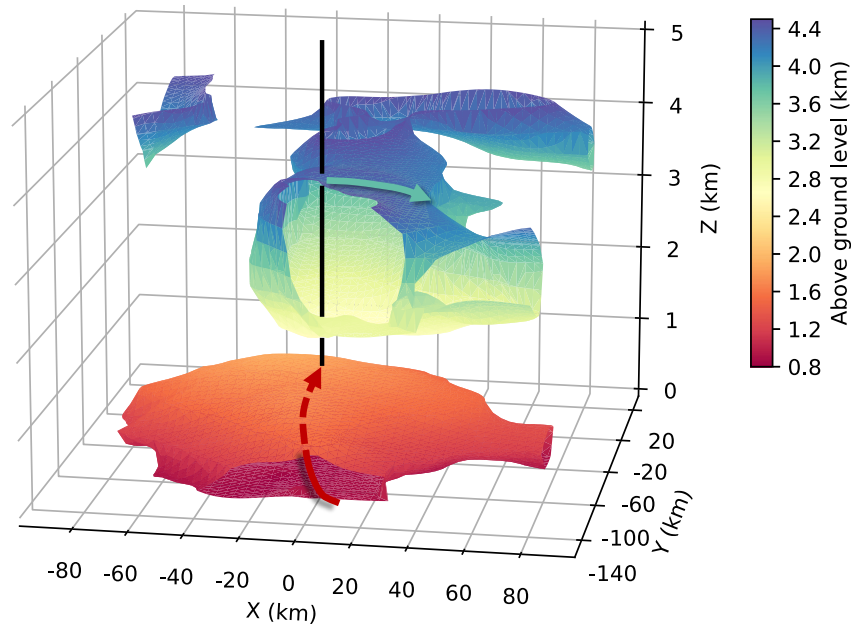


**Figure 13.** 3D structure of the southerly low-level jet (red isosurface,  $19.8 \text{ m s}^{-1}$ ) and mid-tropospheric jet (blue isosurface,  $19.8 \text{ m s}^{-1}$ ) at 2120 LST from variational doppler radar analysis system. Red and green arrows delineate the predominant wind directions within each respective region. The vertical black line indicates the supercell location.

the MTJ (Figure 14b). Evident upward vertical motions occurred in the interface area between these two layers. It is worth noting that the relatively weak magnitude of vertical motions could be possibly due to the coarse resolution (3 km) of the VDRAS model.

We further validate the elevated nature of the convection by calculating the initiation trajectories prior to their entry into the supercell updrafts (Figure 15). Backward trajectories were calculated using a Lagrangian approach, which traces air parcels backward in time, implemented with the Integrated Data Viewer (IDV). These parcels primarily originated from two directions: one group from the southern side near the PBL, and the other from the southwestern side above the PBL between 3 and 4 km, confirming the convection was elevated. Additionally, both groups of trajectories were LLJ-related, indicating the advection of moisture and warm air to the CI location (Figures 9 and 11). Due to the reduced CIN and significant CAPE (Figures 11c and 11f), these parcels experienced abrupt lifting ( $\sim 2.5 \text{ km}$  vertical displacement) in a short period, especially for those originating from the southern side.

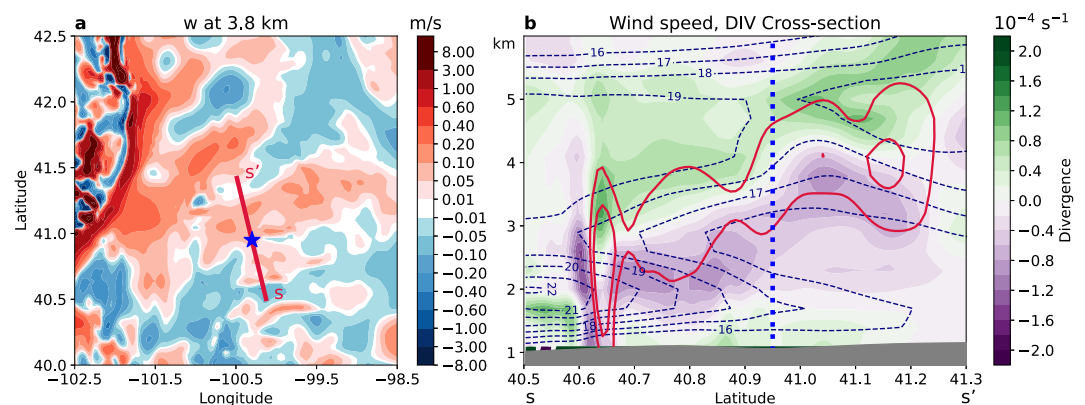


**Figure 14.** (a) Vertical motion at 3.8 km MSL and (b) vertical cross-section of divergence (shading,  $\text{s}^{-1}$ ), vertical motion (red contours, 0.1 and  $0.25 \text{ m s}^{-1}$ ), and wind speed (blue dashed contours) along the red line in (a) at 2120 LST. The blue star in (a) and blue dotted line in (b) represent the C2 location.

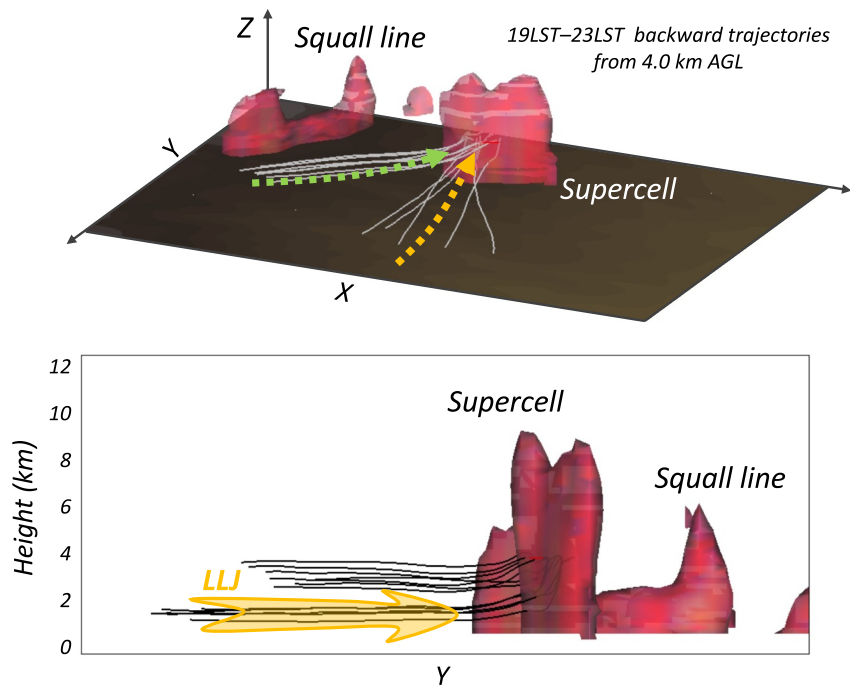


**Figure 15.** Four-hour trajectories calculated backward from the supercell convective updraft cores at 4.0 km AGL at 2300 LST on 23 May 2020. The squall line and supercell are depicted using a 20 dBZ reflectivity isosurface plot with corresponding labels. The green and yellow arrows in the upper panel indicate the two main origins of air parcels while the yellow arrow in the lower panel delineates the location of the low-level jet.

## 5. Conclusions

In the present study, we identified three distinct NCI episodes preceding a squall line in the central Great Plains on 23 May 2020. Our primary focus in this Part 1 paper is on the initiation of a supercell from one NCI. The supercell subsequently merged with the squall line to form a bow echo, which will be examined in Part 2. Utilizing VDRAS to retrieve meteorological and diagnosed fields from radar and surface observations enabled a detailed and refined characterization of the evolution and heterogeneity of both the LLJ and the MTJ. This approach revealed the intricate interplay between the LLJ and MTJ in determining NCI.

During the eastward propagation of the squall line overnight, three distinct convective cells were triggered sequentially downstream. These included a surface-based cell promoted by topographic lifting, a pristine supercell, and linearly arranged cells forming a T-shaped convection pattern with the squall line. Notably, the latter two types exhibited close association with the LLJ.

The initiation mechanisms of the supercell, our focus in this study, are summarized in Figure 16. Before the initiation of the supercell, both large-scale and mesoscale analysis showed the presence of large CIN at lower levels. However, as the nocturnal LLJ strengthened and advected more moisture northward, the low-level environment underwent significant modification, characterized by an increase of approximately  $450 \text{ J kg}^{-1}$  in CAPE and a decrease of around  $30 \text{ J kg}^{-1}$  in CIN. The timing and location of the supercell initiation were determined by the coupling of the LLJ and MTJ. While multiple convergence bands emerged downstream of the heterogeneous LLJ, an elevated CI occurred at locations where persistent ( $>1 \text{ h}$ ) lifting was provided by one of the convergence bands beneath a mid-level divergence band. Further examination indicated that the divergence band coincided with the entrance of the MTJ, which evolved in response to the warm advection associated with the LLJ. In conjunction with MTJ development, a convective jet driven by the approaching squall line was also observed, further complicating the heterogeneity of mid-level airflows.

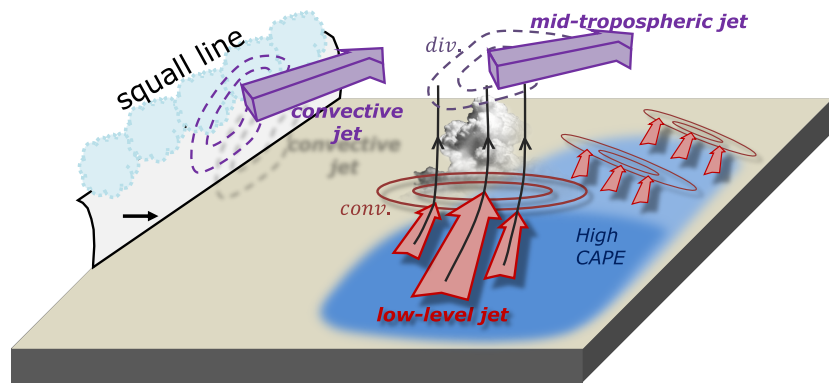


**Figure 16.** Schematic diagram showing the heterogeneous low-level and mid-level flows and the pristine convective initiation ahead of the squall line. Convection occurs at the intersection between the low-level jet's terminus and the entrance of the mid-tropospheric jet, where essential mesoscale lifting and high instability are present.

Subsequently, during the late night (after 2300 LST), the LLJ became more compact and gradually veered from southerly (or southwesterly) to southeasterly. Meanwhile, the convergence band at its terminus shifted to be more prominent on the right flank, facilitating the continuous forward (eastward) initiation of cells, and culminating in the formation of the T-shaped convection.

This study enriched our comprehension of how the LLJ impacts NCI, particularly through its interaction with middle-level winds. Additionally, we underscored the critical role of LLJ heterogeneity in shaping dynamic and thermodynamic processes associated with NCI. Our results suggested a need for a more comprehensive characterization of the three-dimensional structure of the LLJ, especially its relationship with its higher-level winds, which has received comparatively less attention in existing literature. While challenges persist in accurately forecasting NCI over the Great Plains, we are optimistic that advancements can be realized through enhanced understanding of various aspects of the LLJ via extensive observation campaigns and high-resolution numerical modeling.

## Data Availability Statement

The ERA5 reanalysis data used in this study are available from Copernicus Climate Data Store (Hersbach et al., 2020). The NCEP GFS analysis used to drive WRF can be downloaded from <https://rda.ucar.edu/datasets/ds084-1/> (NCEP/National Weather Service/NOAA/U.S. Department of Commerce, 2015). The Next Generation Weather Radar (NEXRAD) data are freely available at <https://aws.amazon.com/public-datasets/nexrad/> (NOAA National Weather Service Radar Operations Center, 1991), the sounding profiles are archived obtained from <https://weather.uwyo.edu/upperair/sounding.html>, and the 5-min ASOS data can be accessed from <https://www.ncei.noaa.gov/products/land-based-station/automated-surface-weather-observing-systems> (NOAA National Centers for Environmental Information, 2021). The IDV is public available (Unidata, 2022) and can be downloaded via <https://downloads.unidata.ucar.edu/idv/>.

## References

- Astling, E. G., Paegle, J., Miller, E., & O'Brien, C. J. (1985). Boundary layer control of nocturnal convection associated with a synoptic scale system. *Monthly Weather Review*, 113(4), 540–552. [https://doi.org/10.1175/1520-0493\(1985\)113<0540:BLCONC>2.0.CO;2](https://doi.org/10.1175/1520-0493(1985)113<0540:BLCONC>2.0.CO;2)
- Augustine, J. A., & Caracena, F. (1994). Lower-tropospheric precursors to nocturnal MCS development over the central United States. *Weather and Forecasting*, 9(1), 116–135. [https://doi.org/10.1175/1520-0434\(1994\)009<0116:LTPTNM>2.0.CO;2](https://doi.org/10.1175/1520-0434(1994)009<0116:LTPTNM>2.0.CO;2)
- Blackadar, A. K. (1957). Boundary layer wind maxima and their significance for the growth of nocturnal inversions. *Bulletin of the American Meteorological Society*, 38(5), 283–290. <https://doi.org/10.1175/1520-0477-38.5.283>
- Bonner, W. D. (1966). Case study of thunderstorm activity in relation to the low-level jet. *Monthly Weather Review*, 94(3), 167–178. [https://doi.org/10.1175/1520-0493\(1966\)094<0167:CSOTAI>2.3](https://doi.org/10.1175/1520-0493(1966)094<0167:CSOTAI>2.3)
- Burrows, D. A., Ferguson, C. R., & Bosart, L. F. (2020). The role of upper-level coupling on great plains low-level jet structure and variability. *Journal of the Atmospheric Sciences*, 77(12), 4317–4335. <https://doi.org/10.1175/JAS-D-20-0059.1>
- Carbone, R. E., & Tuttle, J. D. (2008). Rainfall occurrence in the U.S. warm season: The diurnal cycle. *Journal of Climate*, 21(16), 4132–4146. <https://doi.org/10.1175/2008JCLI2275.1>
- Carbone, R. E., Tuttle, J. D., Ahijevych, D. A., & Trier, S. B. (2002). Inferences of predictability associated with warm season precipitation episodes. *Journal of the Atmospheric Sciences*, 59(13), 2033–2056. [https://doi.org/10.1175/1520-0469\(2002\)059<2033:IOPAWW>2.0](https://doi.org/10.1175/1520-0469(2002)059<2033:IOPAWW>2.0)

## Acknowledgments

This study was supported by the National Natural Science Foundation of China (Grants 424B2033 and 42475002), the Guangdong Major Project of Basic and Applied Basic Research (Grants 2020B0301030004, 2024A1515510005 and 2025A1515011974), projects supported by Southern Marine Science and Engineering Guangdong Laboratory (Zhuhai) (SML2024SP035, SML2024SP012, and 311024001), and the Key Innovation Team of China Meteorological Administration (CMA2023ZD08). We also acknowledge the high-performance computing support from the School of Atmospheric Sciences of Sun Yat-sen University. The authors thank Dr. Yuan Ho (NCAR) for his instruction on backward trajectories (Figure 15) using Integrated Data Viewer (IDV), and NCAR for supporting the first author's visit and for providing computing resources and VDRAS access during his stay. NCAR is sponsored by the National Science Foundation of the United States.

- Chang, S.-F., Liou, Y.-C., Sun, J., & Tai, S.-L. (2016). The implementation of the ice-phase microphysical process into a four-dimensional variational doppler radar analysis system (VDRAS) and its impact on parameter retrieval and quantitative precipitation nowcasting. *Journal of the Atmospheric Sciences*, 73(3), 1015–1038. <https://doi.org/10.1175/JAS-D-15-0184.1>
- Chen, G. T.-J., Wang, C.-C., & Lin, D. T.-W. (2005). Characteristics of low-level jets over northern Taiwan in Mei-Yu season and their relationship to heavy rain events. *Monthly Weather Review*, 133(1), 20–43. <https://doi.org/10.1175/MWR-2813.1>
- Chen, X., Zhao, K., Sun, J., Zhou, B., & Lee, W.-C. (2016). Assimilating surface observations in a four-dimensional variational doppler radar data assimilation system to improve the analysis and forecast of a squall line case. *Advances in Atmospheric Sciences*, 33(10), 1106–1119. <https://doi.org/10.1007/s00376-016-5290-0>
- Coniglio, M. C., Corfidi, S. F., & Kain, J. S. (2011). Environment and early evolution of the 8 May 2009 derecho-producing convective system. *Monthly Weather Review*, 139(4), 1083–1102. <https://doi.org/10.1175/2010MWR3413.1>
- Crook, N. A., & Sun, J. (2004). Analysis and forecasting of the low-level wind during the Sydney 2000 forecast demonstration project. *Weather and Forecasting*, 19(1), 151–167. [https://doi.org/10.1175/1520-0434\(2004\)019<0151:AAFOTL>2.0](https://doi.org/10.1175/1520-0434(2004)019<0151:AAFOTL>2.0)
- Cui, C., Zhou, W., Yang, H., Wang, X., Deng, Y., Wang, X., et al. (2023). Analysis of the characteristics of the low-level jets in the middle reaches of the Yangtze River during the Mei-Yu season. *Advances in Atmospheric Sciences*, 40(4), 711–724. <https://doi.org/10.1007/s00376-022-2107-1>
- Davis, C. A., Manning, K. W., Carbone, R. E., Trier, S. B., & Tuttle, J. D. (2003). Coherence of warm-season continental rainfall in numerical weather prediction models. *Monthly Weather Review*, 131(11), 2667–2679. [https://doi.org/10.1175/1520-0493\(2003\)131<2667:COWCRI>2.0.CO;2](https://doi.org/10.1175/1520-0493(2003)131<2667:COWCRI>2.0.CO;2)
- Du, Y., & Chen, G. (2019). Heavy rainfall associated with double low-level jets over southern China. Part II: Convection initiation. *Monthly Weather Review*, 147(2), 543–565. <https://doi.org/10.1175/MWR-D-18-0102.1>
- Du, Y., & Rotunno, R. (2014). A simple analytical model of the nocturnal low-level jet over the great plains of the United States. *Journal of the Atmospheric Sciences*, 71(10), 3674–3683. <https://doi.org/10.1175/JAS-D-14-0060.1>
- Du, Y., Shen, Y., & Chen, G. (2022). Influence of coastal marine boundary layer jets on rainfall in South China. *Advances in Atmospheric Sciences*, 39(5), 782–801. <https://doi.org/10.1007/s00376-021-1195-7>
- Fritsch, J. M., Kane, R. J., & Chelius, C. R. (1986). The contribution of mesoscale convective weather systems to the warm-season precipitation in the United States. *Journal of Climate and Applied Meteorology*, 25(10), 1333–1345. [https://doi.org/10.1175/1520-0450\(1986\)025<1333:TCOMCW>2.0](https://doi.org/10.1175/1520-0450(1986)025<1333:TCOMCW>2.0)
- Gebauer, J. G., Shapiro, A., Fedorovich, E., & Klein, P. (2018). Convection initiation caused by heterogeneous low-level jets over the great plains. *Monthly Weather Review*, 146(8), 2615–2637. <https://doi.org/10.1175/MWR-D-18-0002.1>
- Geerts, B., Parsons, D., Ziegler, C. L., Weckwerth, T. M., Biggerstaff, M. I., Clark, R. D., et al. (2017). The 2015 plains elevated convection at night field project. *Bulletin of the American Meteorological Society*, 98(4), 767–786. <https://doi.org/10.1175/BAMS-D-15-00257.1>
- Hersbach, H., Bell, B., Berrisford, P., Hirahara, S., Horányi, A., Muñoz-Sabater, J., et al. (2020). The ERA5 global reanalysis. *Quarterly Journal of the Royal Meteorological Society*, 146(730), 1999–2049. <https://doi.org/10.1002/qj.3803>
- Higgins, R. W., Yao, Y., Yarosh, E. S., Janowiak, J. E., & Mo, K. C. (1997). Influence of the great plains low-level jet on summertime precipitation and moisture transport over the central United States. *Journal of Climate*, 10(3), 481–507. [https://doi.org/10.1175/1520-0442\(1997\)010<0481:IOTGPL>2.0](https://doi.org/10.1175/1520-0442(1997)010<0481:IOTGPL>2.0)
- Jiang, X., Lau, N.-C., Held, I. M., & Ploshay, J. J. (2007). Mechanisms of the great plains low-level jet as simulated in an AGCM. *Journal of the Atmospheric Sciences*, 64(2), 532–547. <https://doi.org/10.1175/JAS3847.1>
- Liu, X., Luo, Y., Huang, L., Zhang, D., & Guan, Z. (2020). Roles of double low-level jets in the generation of coexisting inland and coastal heavy rainfall over South China during the presummer rainy season. *Journal of Geophysical Research: Atmospheres*, 125(18), e2020JD032890. <https://doi.org/10.1029/2020JD032890>
- Luo, Y., & Du, Y. (2023). The roles of low-level jets in “21-7” Henan extremely persistent heavy rainfall event. *Advances in Atmospheric Sciences*, 40(3), 350–373. <https://doi.org/10.1007/s00376-022-2026-1>
- Maddox, R. A. (1983). Large-scale meteorological conditions associated with midlatitude, mesoscale convective complexes. *Monthly Weather Review*, 111(7), 1475–1493. [https://doi.org/10.1175/1520-0493\(1983\)111<1475:LSMCAW>2.0.CO;2](https://doi.org/10.1175/1520-0493(1983)111<1475:LSMCAW>2.0.CO;2)
- Maddox, R. A. (1980). Mesoscale convective complexes. *Bulletin of the American Meteorological Society*, 61(11), 1374–1387. [https://doi.org/10.1175/1520-0477\(1980\)061<1374:MCC>2.0](https://doi.org/10.1175/1520-0477(1980)061<1374:MCC>2.0)
- Moore, J. T., Glass, F. H., Graves, C. E., Rochette, S. M., & Singer, M. J. (2003). The environment of warm-season elevated thunderstorms associated with heavy rainfall over the central United States. *Weather and Forecasting*, 18(5), 861–878. [https://doi.org/10.1175/1520-0434\(2003\)018<0861:TEOWET>2.0](https://doi.org/10.1175/1520-0434(2003)018<0861:TEOWET>2.0)
- NCEP/National Weather Service/NOAA/U.S. Department of Commerce. (2015). NCEP GFS 0.25 degree global forecast grids historical archive [Dataset]. *Research Data Archive at the National Center for Atmospheric Research, Computational and Information Systems Laboratory*. <https://doi.org/10.5065/D65D8PWK>
- NOAA National Centers for Environmental Information. (2021). Automated surface/weather observing systems (ASOS/AWOS) [Dataset]. NOAA. Retrieved from <https://www.ncei.noaa.gov/products/land-based-station/automated-surface-weather-observing-systems>
- NOAA National Weather Service Radar Operations Center. (1991). NOAA Next generation radar (NEXRAD) level 2 base data [Dataset]. *NOAA National Centers for Environmental Information*. <https://doi.org/10.7289/V5W9574V>
- Pitchford, K. L., & London, J. (1962). The low-level jet as related to nocturnal thunderstorms over midwest United States. *Journal of Applied Meteorology*, 1(1), 43–47. [https://doi.org/10.1175/1520-0450\(1962\)001<0043:TLLJAR>2.0](https://doi.org/10.1175/1520-0450(1962)001<0043:TLLJAR>2.0)
- Pu, B., & Dickinson, R. E. (2014). Diurnal spatial variability of great plains summer precipitation related to the dynamics of the low-level jet. *Journal of the Atmospheric Sciences*, 71(5), 1807–1817. <https://doi.org/10.1175/JAS-D-13-0243.1>
- Rasmusson, E. M. (1967). Atmospheric water vapor transport and the water balance of North America. Part I: Characteristics of the water vapor flux field. *Monthly Weather Review*, 95(7), 403–426. [https://doi.org/10.1175/1520-0493\(1967\)095<0403:AWVTAT>2.3](https://doi.org/10.1175/1520-0493(1967)095<0403:AWVTAT>2.3)
- Reif, D. W., & Bluestein, H. B. (2017). A 20-year climatology of nocturnal convection initiation over the central and southern great plains during the warm season. *Monthly Weather Review*, 145(5), 1615–1639. <https://doi.org/10.1175/MWR-D-16-0340.1>
- Reif, D. W., & Bluestein, H. B. (2018). Initiation mechanisms of nocturnal convection without nearby surface boundaries over the central and southern great plains during the warm season. *Monthly Weather Review*, 146(9), 3053–3078. <https://doi.org/10.1175/MWR-D-18-0040.1>
- Smith, E. N., Gebauer, J. G., Klein, P. M., Fedorovich, E., & Gibbs, J. A. (2019). The great plains low-level jet during PECAN: Observed and simulated characteristics. *Monthly Weather Review*, 147(6), 1845–1869. <https://doi.org/10.1175/MWR-D-18-0293.1>
- Sun, J., & Crook, N. A. (1997). Dynamical and microphysical retrieval from doppler radar observations using a cloud model and its adjoint. Part I: Model development and simulated data experiments. *Journal of the Atmospheric Sciences*, 54(12), 1642–1661. [https://doi.org/10.1175/1520-0469\(1997\)054<1642:DAMRFD>2.0](https://doi.org/10.1175/1520-0469(1997)054<1642:DAMRFD>2.0)



- Sun, J., & Crook, N. A. (1998). Dynamical and microphysical retrieval from doppler radar observations using a cloud model and its adjoint. Part II: Retrieval experiments of an observed Florida convective storm. *Journal of the Atmospheric Sciences*, 55(5), 835–852. [https://doi.org/10.1175/1520-0469\(1998\)055<0835:DAMRFD>2.0.CO;2](https://doi.org/10.1175/1520-0469(1998)055<0835:DAMRFD>2.0.CO;2)
- Sun, J., Li, R., Zhang, Q., Trier, S. B., Ying, Z., & Xu, J. (2023). Mesoscale factors contributing to the extreme rainstorm on 20 July 2021 in Zhengzhou, China, as revealed by rapid update 4Dvar analysis. *Monthly Weather Review*, 151(8), 2153–2176. <https://doi.org/10.1175/MWR-D-22-0337.1>
- Surcel, M., Berenguer, M., & Zawadzki, I. (2010). The diurnal cycle of precipitation from continental radar mosaics and numerical weather prediction models. Part I: Methodology and seasonal comparison. *Monthly Weather Review*, 138(8), 3084–3106. <https://doi.org/10.1175/2010MWR3125.1>
- Tai, S.-L., Liou, Y.-C., Sun, J., & Chang, S.-F. (2017). The development of a terrain-resolving scheme for the forward model and its adjoint in the four-dimensional variational doppler radar analysis system (VDRAS). *Monthly Weather Review*, 145(1), 289–306. <https://doi.org/10.1175/MWR-D-16-0092.1>
- Trier, S. B., Davis, C. A., Ahijevych, D. A., & Manning, K. W. (2014). Use of the parcel buoyancy minimum to diagnose simulated thermodynamic destabilization. Part I: Methodology and case studies of MCS initiation environments. *Monthly Weather Review*, 142(3), 945–966. <https://doi.org/10.1175/MWR-D-13-00272.1>
- Trier, S. B., Davis, C. A., Ahijevych, D. A., Weisman, M. L., & Bryan, G. H. (2006). Mechanisms supporting long-lived episodes of propagating nocturnal convection within a 7-day WRF model simulation. *Journal of the Atmospheric Sciences*, 63(10), 2437–2461. <https://doi.org/10.1175/JAS3768.1>
- Trier, S. B., Kehler, S. D., & Hanesiak, J. (2020). Observations and simulation of elevated nocturnal convection initiation on 24 June 2015 during PECAN. *Monthly Weather Review*, 148(2), 613–635. <https://doi.org/10.1175/MWR-D-19-0218.1>
- Trier, S. B., & Parsons, D. B. (1993). Evolution of environmental conditions preceding the development of a nocturnal mesoscale convective complex. *Monthly Weather Review*, 121(4), 1078–1098. [https://doi.org/10.1175/1520-0493\(1993\)121<1078:EOECPT>2.0](https://doi.org/10.1175/1520-0493(1993)121<1078:EOECPT>2.0)
- Trier, S. B., Wilson, J. W., Ahijevych, D. A., & Sobash, R. A. (2017). Mesoscale vertical motions near nocturnal convection initiation in PECAN. *Monthly Weather Review*, 145(8), 2919–2941. <https://doi.org/10.1175/MWR-D-17-0005.1>
- Tuttle, J. D., & Davis, C. A. (2006). Corridors of warm season precipitation in the central United States. *Monthly Weather Review*, 134(9), 2297–2317. <https://doi.org/10.1175/MWR3188.1>
- Uccellini, L. W., & Johnson, D. R. (1979). The coupling of upper and lower tropospheric jet streaks and implications for the development of severe convective storms. *Monthly Weather Review*, 107(6), 682–703. [https://doi.org/10.1175/1520-0493\(1979\)107<0682:TCOUAL>2.0.CO;2](https://doi.org/10.1175/1520-0493(1979)107<0682:TCOUAL>2.0.CO;2)
- Unidata. (2022). Integrated data viewer (IDV) version 6.1 [Computer software]. UCAR/Unidata Program Center. <https://doi.org/10.5065/D6RN35XM>
- Wallace, J. M. (1975). Diurnal variations in precipitation and thunderstorm frequency over the conterminous United States. *Monthly Weather Review*, 103(5), 406–419. [https://doi.org/10.1175/1520-0493\(1975\)103<0406:DVIPAT>2.0.CO;2](https://doi.org/10.1175/1520-0493(1975)103<0406:DVIPAT>2.0.CO;2)
- Weckwerth, T. M., Hanesiak, J., Wilson, J. W., Trier, S. B., Degelia, S. K., Gallus, W. A., et al. (2019). Nocturnal convection initiation during PECAN 2015. *Bulletin of the American Meteorological Society*, 100(11), 2223–2239. <https://doi.org/10.1175/BAMS-D-18-0299.1>
- Wilson, J. W., & Roberts, R. D. (2006). Summary of convective storm initiation and evolution during IHOP: Observational and modeling perspective. *Monthly Weather Review*, 134(1), 23–47. <https://doi.org/10.1175/MWR3069.1>
- Xiao, X., Sun, J., Chen, M., Qie, X., Wang, Y., & Ying, Z. (2017). The characteristics of weakly forced mountain-to-plain precipitation systems based on radar observations and high-resolution reanalysis. *Journal of Geophysical Research: Atmospheres*, 122(6), 3193–3213. <https://doi.org/10.1002/2016JD025914>
- Zhang, F., Li, G., & Yue, J. (2019). The moisture sources and transport processes for a sudden rainstorm associated with double low-level jets in the northeast Sichuan basin of China. *Atmosphere*, 10(3), 160. <https://doi.org/10.3390/atmos10030160>
- Zhang, L., Sun, J., Ying, Z., & Xiao, X. (2021). Initiation and development of a squall line crossing Hangzhou Bay. *Journal of Geophysical Research: Atmospheres*, 126(1), e2020JD032504. <https://doi.org/10.1029/2020jd032504>
- Zhang, M., & Meng, Z. (2019). Warm-sector heavy rainfall in southern China and its WRF simulation evaluation: A low-level-jet perspective. *Monthly Weather Review*, 147(12), 4461–4480. <https://doi.org/10.1175/MWR-D-19-0110.1>